RESEARCH ARTICLE

Functional Materials for Energy Harvesting

Energy & Environmental Materials WILEY

Bioinspired Flexible and Stretchable Coil Structure from $Ti_3C_2T_x$ MXene/AgNPs-Functionalized Piezoelectric Nanofibers for Enhanced Energy Harvesting

*Fatemeh Mokhtari**, *Alexander Volodine*, *Olivier Deschaume*, *Carmen Bartic*, *Albert de Kogel*, *Xuehang Wang*, *and Russell J. Varley**

The growing popularity of smart electronics in wearables, the Internet of Things (IoT), soft robotics, and biomedical implants simultaneously demands more reliable and durable power sources. However, limitations on battery life continue to compromise reliability, prompting the search for sustainable solutions for flexible, self-powered systems. In this work, stretchable self-powered piezoelectric nanogenerators have been designed from functionalized piezoelectric nanofibers with a bioinspired coiled helical microstructure. Composed of two-dimensional (2D) $Ti_3C_2T_x$ MXene and silver nanoparticles (AgNPs) embedded in a poly(vinylidene fluoride-co-trifluoroethylene) (P(VDF-TrFE)) matrix, the coiled structure achieves a mechanoelectrical energy conversion efficiency of 17%, and a power output of 6.6 mW cm^{-3} at 50% strain, twice the performance of similarly coiled structures. These improvements were attributed to the threefold increase in the piezoelectric coefficient through the addition of 1 wt% AgNPs to the P(VDF-TrFE)/MXene (0.1 wt%) and the coiled structure further enhancing β-phase formation reaching up to 70%. An electrospun mat sensor with dimensions of 2 × 3 cm generated 3 V at 1 Hz under an applied pressure of 7 kPa. The coil compact and lightweight design enables seamless integration into miniaturized electronics and wearable biomedical devices, promising a sustainable, battery-free power solution.

1. Introduction

Stretchable self-powered systems are of great interest for sustainable and efficient energy solutions in wearable electronics, autonomous sensors, human–computer interaction systems, and implantable micropower medical devices.[1] This growing demand has driven significant advancements, focusing on material innovation and structural optimization to enhance the efficiency of converting mechanical energy into electrical signals in piezoelectric materials.[2]

The synergies afforded through these approaches combined with miniaturization, is enabling piezoelectric generators to function efficiently in low frequency environments. When fully integrated and compatible at the systems level, these devices are highly promising for a wide range of low-power applications, particularly in medical devices.[3] Implantable medical devices (IMDs) are becoming widespread, but often depend upon external power sources, raising concerns about efficiency, limited lifespan, and patient comfort. To address these issues, piezoelectric materials offer a unique solution by harnessing biomechanical energy sources and transforming them into electrical energy, enabling IMDs such as pacemakers,[4] neural stimulators,[5] cochlear implants[6] and other devices to operate independently.[7] Furthermore, increasing amounts of electronic waste, predicted to reach 82 million tons by 2030, emphasizes the need to develop more energy efficient, durable, and sustainable medical electronics.[8] Technologies such as self-powered piezoelectric sensors address this need by generating their own energy from body movements, reducing reliance on disposable batteries and minimizing electronic waste over time.

Poly(vinylidene fluoride-co-trifluoroethylene) (P(VDF-TrFE)) is a broadly recognized piezoelectric polymer used in composite systems due to its favorable electroactive properties.[9] It is particularly well-suited for electrospinning, as it efficiently forms the electroactive β-phase than polyvinylidene fluoride (PVDF).[10] Although piezoelectric polymers are highly valued for their flexibility and ease of processing, their inherently low piezoelectric charge coefficients (d), compared with ceramic based piezoelectric materials, generate weak electrical signals that are often challenging to detect. As a result, performance enhancement typically necessitates the use of signal amplification

Dr. F. Mokhtari
Department of Materials Engineering, KU Leuven, Leuven 3001, Belgium
E-mail: fatemeh.mokhtari@kuleuven.be
Dr. A. Volodine
Department of Physics and Astronomy, KU Leuven, Celestijnenlaan 200D, Leuven 3001, Belgium
Dr. O. Deschaume, Prof. C. Bartic
Department of Physics and Astronomy, Laboratory for Soft Matter and Biophysics, KU Leuven, Celestijnenlaan 200D, Leuven 3001, Belgium
A. de Kogel, Prof. X. Wang
Department of Radiation Science and Technology, Delft University of Technology, Delft 2629 JB, The Netherlands
Prof. R. J. Varley
School of Engineering, RMIT University, Melbourne, Victoria 3001, Australia
E-mail: russell.varley2@rmit.edu.au
The ORCID identification number(s) for the author(s) of this article can be found under https://doi.org/10.1002/eem2.70348.

DOI: 10.1002/eem2.70348

strategies such as the incorporation of inorganic and functional fillers,[11] or post-treatment techniques.[9] Frequently used fillers such as zinc oxide (ZnO),[12] silver nanoparticles (AgNP),[13] MXene,[14] barium titanate,[15] reduced graphene oxide,[16] and molybdenum disulfide (MoS_2),[17] significantly enhance performance by increasing charge trapping and electrical conductivity. Nonetheless, selection of piezoelectric materials and fillers for composite structures is influenced by several critical factors, including operating frequency, mechanical flexibility, spatial constraints, piezoelectric performance, environmental stability, biocompatibility, fabrication complexity, cost considerations, and the specific requirements of the intended application sector.[18]

MXenes are two-dimensional (2D) materials known for their excellent dispersion in solvents, high electrical conductivity, and abundant surface functional groups. Their general chemical formula is $M_{n+1}X_nT_x$ ($n = 1–3$), where M denotes an early transition metal, X represents carbon and/or nitrogen, and T_x refers to surface terminations such as OH, O, Cl, and F.[19] Among the various MXene compounds, $Ti_3C_2T_x$ has been the most extensively investigated for applications in piezoelectric generators due to its high electrical conductivity, which consequently enhances the dielectric constant, charge-inducing, and charge-trapping capabilities of piezoelectric polymers.[20,21] $Ti_3C_2T_x$ MXene flakes, with polar functional groups, provide strong electrostatic interactions with PVDF-TrFE, which effectively stabilize the polarization of polymer chains and lead to significantly enhanced energy harvesting performance.[22] Silver is a highly promising material for biomedical applications owing to its broad-spectrum antibacterial efficacy, excellent electrical conductivity, and cost-effectiveness[23] making it a valuable additive when incorporated into piezoelectric fibers.[24] Furthermore, silver nanoparticles improve the interfacial coupling with PVDF, helping the polymer chains adopt the all-trans conformation, a highly ordered, straight alignment that maximizes dipole orientation and enhances the PVDF piezoelectric performance.[13]

In addition to the composition of the nanofibers, the structural design and geometry play a key role in determining overall performance of piezoelectric nanogenerators. The most common of which adopt a sandwich structure, consisting of a thin piezoelectric layer sandwiched between two electrodes on the top and bottom. However, to achieve higher efficiencies, further innovation is required. Piezoelectric structures are typically arranged in thin films, nanofibers mats, and nanoyarns[25] to enhance flexibility and strain response, while porous foams[26] and core-shell fibers[27] improve the lightweight and charge separation properties. In addition, coating piezoelectric materials on an elastic substrate within an "island-bridge" structure utilizes the inherent stretchable properties of these systems.[28] However, these properties are constrained by the mechanical properties of the materials employed, thereby limiting the attainable deformation or strain. This has led to the development of more stretchable structures that are wavy,[29] helical or coiled[30] or are based upon origami/kirigami,[31] which improve flexibility and wearability, but also seek to improve mechanoelectrical conversion.

The wavy pattern formed by depositing PVDF piezoelectric layers onto template-grooved substrates under applied force creates a wavy structure;[32] however, since this structure is not fixed by temperature, it may exhibit reduced stability and has inherent limitations in stretchability. A disadvantage of origami inspired structures is their out-of-plane deformation during stretching, which results in uneven stress distributions reducing the efficiency of piezoelectric nanogenerators. This leads to mechanical instability, integration challenges, and inconsistent electrical output, limiting device reliability and performance.[33]

The bioinspired coil-shaped structure of piezoelectric nanofibers mimics natural helices such as DNA, plant tendrils, and the cochlea, which are optimized for flexibility and energy efficiency. In a coil design, the transformation of 1D nanofibers into helical yarns through a twisting process is a straightforward and efficient strategy. Indeed, carbon nanotube coils encapsulated in a silicone tube have been shown to generate electrical charge, which could be transferred to cardiac implantable electronic devices via a sodium chloride solution.[34] Despite its excellent efficiency, fabrication challenges, including the risk of leakage, inhibited further development.

Introducing shape chirality, such as helical geometries, can significantly enhance mechanical performance and flexibility. Yarn structures composed of hierarchically arranged fibers in helical formations exhibit improved strength and elongation due to the orientation and rearrangement of polymer chains and inter-fiber interactions under external forces during the twisting process.[35,36] The twisting of nanofibers strips into a coil structure results in a maximum strain to failure of approximately 700%, which is about 30% higher than that of the untwisted strips. This improvement is attributed to the structural geometry and enhanced toughness from fiber interactions during the twisting process.[30]

The piezoelectric coil structure offers the advantage of a controllable power generation system during stretching and release, which can improve coupling and enhance power efficiency. While recent studies have predominantly focused on single-function strategies to improve nanogenerator performance, this paper investigates a dual-function approach that integrates a modified nanofibers with a coiled structural design to simultaneously enhance piezoelectric activity and mechanical flexibility, overcoming the limitations of a traditional sandwich structure. In this study, $Ti_3C_2T_x$ MXene and AgNPs are incorporated as fillers into PVDF-TrFE nanofibers to enhance their piezoelectric performance. The piezoelectric performance was evaluated using two structural designs, a flat electrospun mat and a coil structure. For the flat mat, the output voltage was characterized as a function of sample dimensions and applied force. In the coil structure mechanical energy is effectively converted into electrical energy under varying strain conditions. Both configurations, together with their respective measurement methods, demonstrate strong potential for integration into pacemaker systems by providing adequate power for recharging low-power components even under minimal mechanical deformation.

2. Results and Discussion

2.1. Morphological and Structural Characterization of the Nanofibers

Mats were obtained via electrospinning of P(VDF-TrFE) suspensions including MXene (0.1 wt%) and AgNPs (1 wt%). Our previous research demonstrated that a MXene concentration of 0.1 wt% yielded the highest effective piezoelectric coefficient (d_{33}) of 1.8 pC/N and the highest dielectric constant (ε) of 34.[14] Incorporating 1 wt% AgNPs significantly increased conductivity, imparted an antibacterial effect, and enhanced piezoelectric performance.[37,38] Mats of varying thicknesses were then cut into ribbons with a width of 1 cm for the twisting process (**Figure 1a–c**). Adding MXene/AgNPs as conductive fillers enhanced the charge density and static electric field strength during electrospinning, leading to an intensification of the extensional flow of P(VDF-TrFE) chains and reducing the nanofibers diameter from 560 to

313 nm (Figure 1d,e). As the electrospinning time was increased from 30 to 120 min, the mat thickness increased, in turn broadening the outer coil diameter from 343 to 595 μm (Figure 1f).

By integrating hybrid techniques that combine traditional twisting methods with nanotechnology, innovative coil structures are achieved. This combined approach enhances tensile strength, flexibility, and overall durability. Figure 1g,h shows SEM micrographs of random nanofibers mats and a fabricated coil. The electrospun coil features a Z-twisted structure along its length. During twisting, the applied torque stretches the nanofibers, prompting them to reorient toward the loading direction and enhancing fiber alignment.[39] The coil forms from the additional twist applied to the electrospun mat strip and consistent uniformity along its entire length is observed. High-magnification images demonstrate that nanofibers alignment is retained through both twisting and overtwisting. Notably, even after significant twisting, the nanofibers remain continuous and show no signs of failure, highlighting their exceptional flexibility and durability (Figure 1h).

As a result of increasing electrospinning time, the number of twists per meter (TPM) decreased from 4636 to 3056 (**Figure 2**a). A reduction in mat thickness after 40 mins electrospinning can be attributed to charge buildup on the collector surface, disrupting uniform fiber deposition. Moreover, as the mat reaches a critical thickness, it begins to electrically insulate the collector, further hindering effective fiber deposition. The FTIR result of P(VDF-TrFE) nanofibers containing MXene and AgNPs exhibited a peak at 840 cm^{-1}, corresponding to the β--crystalline phase (Figure 2b) while silver nanoparticles displayed a prominent peak at 1384 cm^{-1}.[37]

The β-phase is the most critical phase in PVDF, as its arrangement of electronegative fluorine and electropositive hydrogen on opposite sides of the carbon backbone produces a strong net dipole moment, enabling PVDF characteristic piezoelectric behavior. The addition of fillers enhances crystallization, boosting the β-phase content by up to 30% higher than that of pure P(VDF-TrFE). As confirmed by FTIR studies, the hydrogen bonding between MXene flakes and polymer chains contributes to the increase in the β content.[40] The increased β-phase

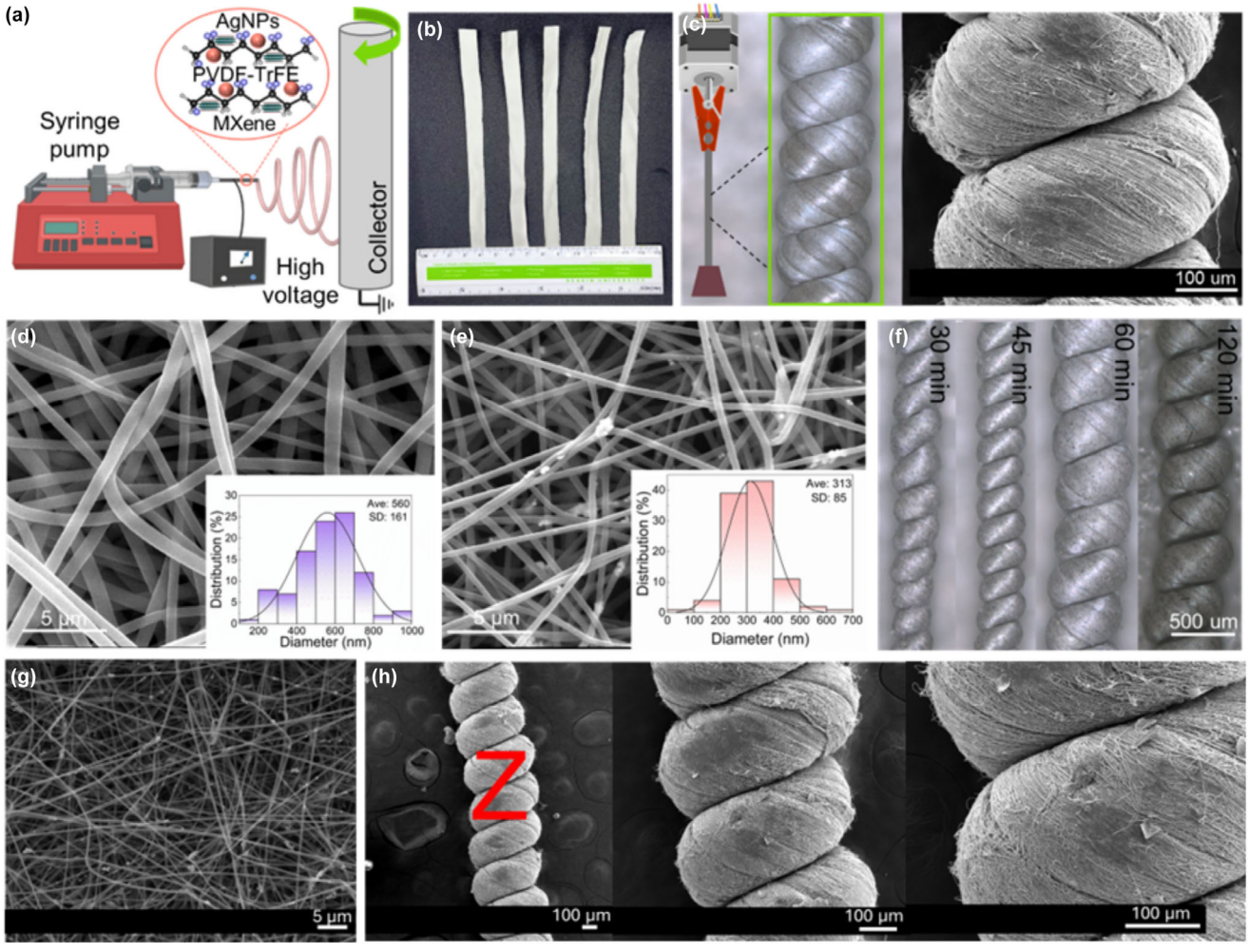

Figure 1. a) Schematic of the electrospinning process; b) electrospun mats cut into 100 mm × 10 mm strips; c) twisting applied using a stepper motor and a hanging weight; SEM images of the poly(vinylidene fluoride-co-trifluoroethylene) (P(VDF-TrFE)) nanofibers containing d) P(VDF-TrFE), e) MXene/silver nanoparticles (AgNPs); and f) optical microscope image of coils obtained from mats with different spinning times, g) SEM micrographs of the random P(VDF-TrFE)/MXene/AgNPs nanofibers, and h) SEM micrographs of Z twist-induced coils fabricated from random nanofibers shown in different magnifications.

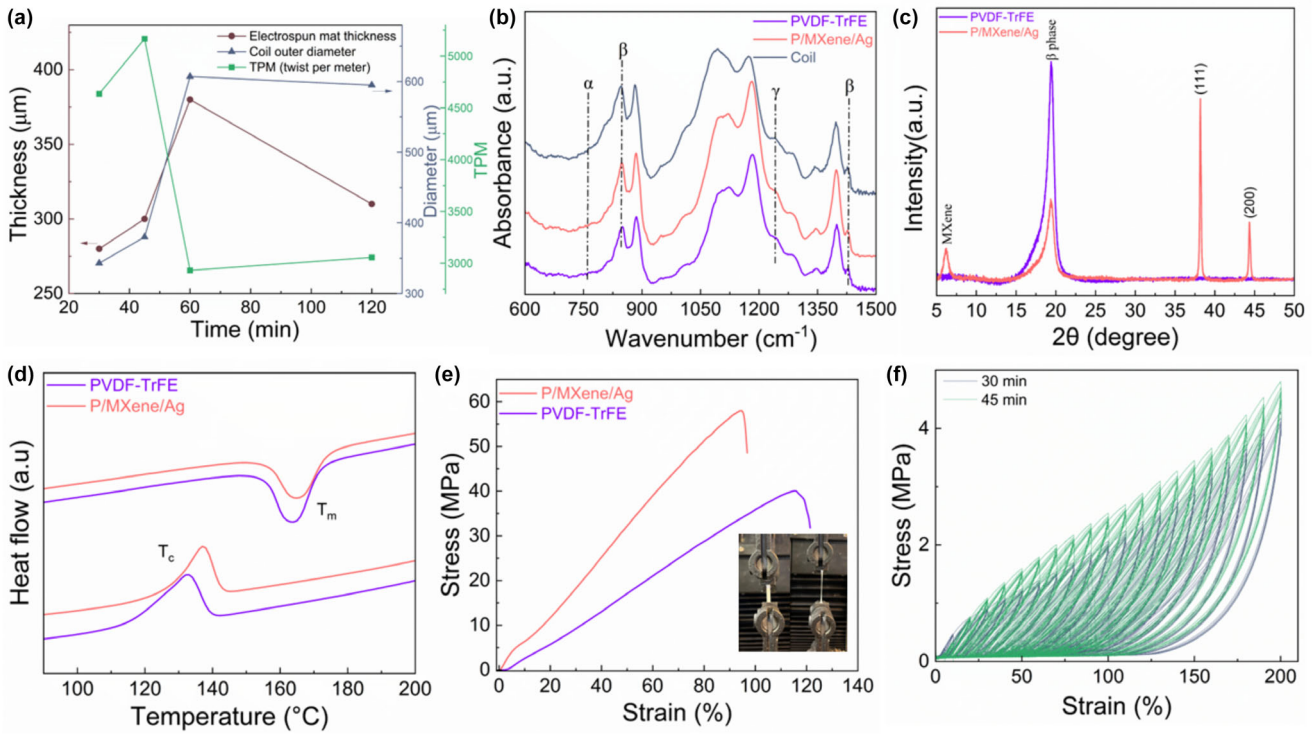

Figure 2. a) Variation of mat thickness and coil diameter and twists per meter (TPM) over different electrospinning time, characterization electrospun mat of pure poly(vinylidene fluoride-co-trifluoroethylene) (P(VDF-TrFE)) and composite containing MXene/silver nanoparticles (AgNPs): b) Fourier-transform infrared (FTIR) spectra, c) X-ray diffraction (XRD) pattern, d) Differential scanning calorimetry (DSC) heating profile, e) tensile stress–strain curves of electrospun mats, and f) Load–unload response of coil obtained from electrospun mats of P(VDF-TrFE)/MXene/AgNps after 30 and 45 min electrospinning, subjected to 200% strain.

formation is attributed to enhanced dipole alignment and fiber stretching along the axial direction during coil fabrication.[15] Furthermore, the annealing process,[41] performed to permanently set the twisted shape of the coil, further enhanced crystallinity and β-phase content leading to a 70% β-phase content in the nanofiber coil structure (Equation S1, Supporting Information).

The presence of MXene in nanofibers was confirmed by X-ray diffraction (XRD) ($2\theta = 6.9°$) (Figure 2c). The sharp diffraction peak at 20° corresponds to the diffraction from the (110) and (200) lattice planes of β- P(VDF-TrFE).[42] The AgNPs exhibited characteristic peaks at 2θ of 38.1° and 44.1°, conforming to the (111) and (200) crystal planes of their face-centered cubic structure.[43] Figure 2d displays the DSC melting curves of P(VDF-TrFE) nanofibers both with and without MXene/AgNPs. The nanofibers display an endothermic melting transition between 160 and 166 °C, with the melting peak shifting to higher temperatures as the MXene and AgNPs concentrations increase. Upon cooling from the melt, the crystallization temperature (T_c) increases from 133 °C for pure P(VDF-TrFE) to 137 °C for nanofibers containing MXene/AgNPs. This elevation in T_c indicates heterogeneous nucleation induced by the fillers, likely resulting in reduced crystallite size.[20] Furthermore, the narrowing of the T_c peak suggests a more uniform distribution of crystallites. Overall, DSC analysis revealed that the crystallinity of pure P(VDF-TrFE) nanofibers was 53.4% increased to 65.7% upon addition of MXene/AgNPs.[37]

The uniform dispersion of MXene/AgNPs, in the nanofiber, along with enhanced interfacial bonding with P(VDF-TrFE), resulted in a twofold increase in Young's modulus and boosted the tensile strength from 40 to 58 MPa (Figure 2e). Figure 2f presents cyclic loading-unloading tensile testing carried out on coil structures derived from the electrospun mats after 30 and 45 min of electrospinning where both samples displayed similar levels of hysteresis. While the coil sample after 45 min electrospinning displays a higher TPM, it requires more stress for deformation. The results exhibit hysteresis, where the strain returns to zero after unloading at strains up to approximately 200%, indicating elastic deformation. Plastic deformation happens beyond this strain threshold. The deformation mechanism can be attributed to the initial separation of adjacent coil surfaces, followed by the incremental unwinding of the coils until the structure is fully extended.

2.2. Electrical and Electromechanical Characterization of Nanofibers

The local mechanical response of the materials to an applied electric field was measured using piezoelectric force microscopy (PFM). In **Figure 3**a–d, the PFM images of P(VDF-TrFE)/MXene nanofibers with different AgNPs concentrations (0, 0.5, 1 and 2 wt%) where the piezoelectric response (PR) images clearly highlight the non-uniform distribution along the axis of the fibers and their widths. To obtain satisfactory data for comparative evaluation, for each of the four fibers, the average PR values were calculated from six cross-sections (Figure 3a_i–d_i) over the surface of the samples. Based on the results of quantitative

calibration of PR on a single fiber, the highest PR value was obtained for fibers with 1 wt% AgNPs while the lowest was observed for 2 wt% AgNPs.

The parameters d_{33} and d_{31} are coefficients used to describe the behavior of the mats for longitudinal and transverse modes and converting the mechanical energy into electrical energy effectively. The d_{33} coefficient of the P(VDF-TrFE)/MXene composite mat was measured to be 4 pC/N. Under identical experimental conditions, the piezoelectric response of the composite mat was significantly enhanced with the incorporation of an optimal amount of Ag nanoparticles. A maximum d_{33} value of 11.3 pC/N was achieved at 1 wt% AgNPs. However, when the AgNPs content exceeded 2 wt%, the d_{33} decreased (Figure 3e) similar to previous observations for the P(VDF-TrFE)/$BaTiO_3$ system modified with MXene.[44]

MXenes can form a lamellar structure in composites and improve their interfacial polarization. Considering the coordination effect among fillers of different dimensions, adding MXene and other conductive fillers such as AgNPs with different dimensions to the P(VDF-TrFE) matrix will greatly improve the dispersion of MXene, thereby enhancing the composites' performance.[45] MXene flakes contribute to better reinforcement with the polymer matrix due to their high surface area, which facilitates improved interaction of -F and -OH bonds on the surface of MXene, with the C–F and C–H bonds of the P(VDF-TrFE) molecules,[14] promoting β-phase crystallization (Figure 2b) and efficient stress transfer. The incorporation of AgNPs, leading to the Coulomb blockade effect and the formation of additional heterogeneous nucleation sites, can inhibit charge transport in the polymer matrix. The synergistic effect of fillers enhances the interfacial interaction between the nanoparticles and the P(VDF-TrFE) matrix, increases conductivity,[23] and promotes the alignment and development of microscopic dipoles during electrospinning, as well as the formation of a microcapacitor network.[14] These effects collectively increase the dielectric constant of the composite and enhance the piezoelectric coefficient (Equation S2, Supporting Information).[46] However, above 1 wt.% AgNPs, the percolation threshold is surpassed, leading to a reduction in the d_{33} and d_{31} coefficients (Figure 3e,f).

The value of the axial strain-induced effect expressed in the piezoelectric coefficient d_{33} is more than that of the transverse coefficient d_{31}. A high d_{33} value indicates strong piezoelectric sensitivity in the longitudinal direction, making the sensor particularly well-suited for

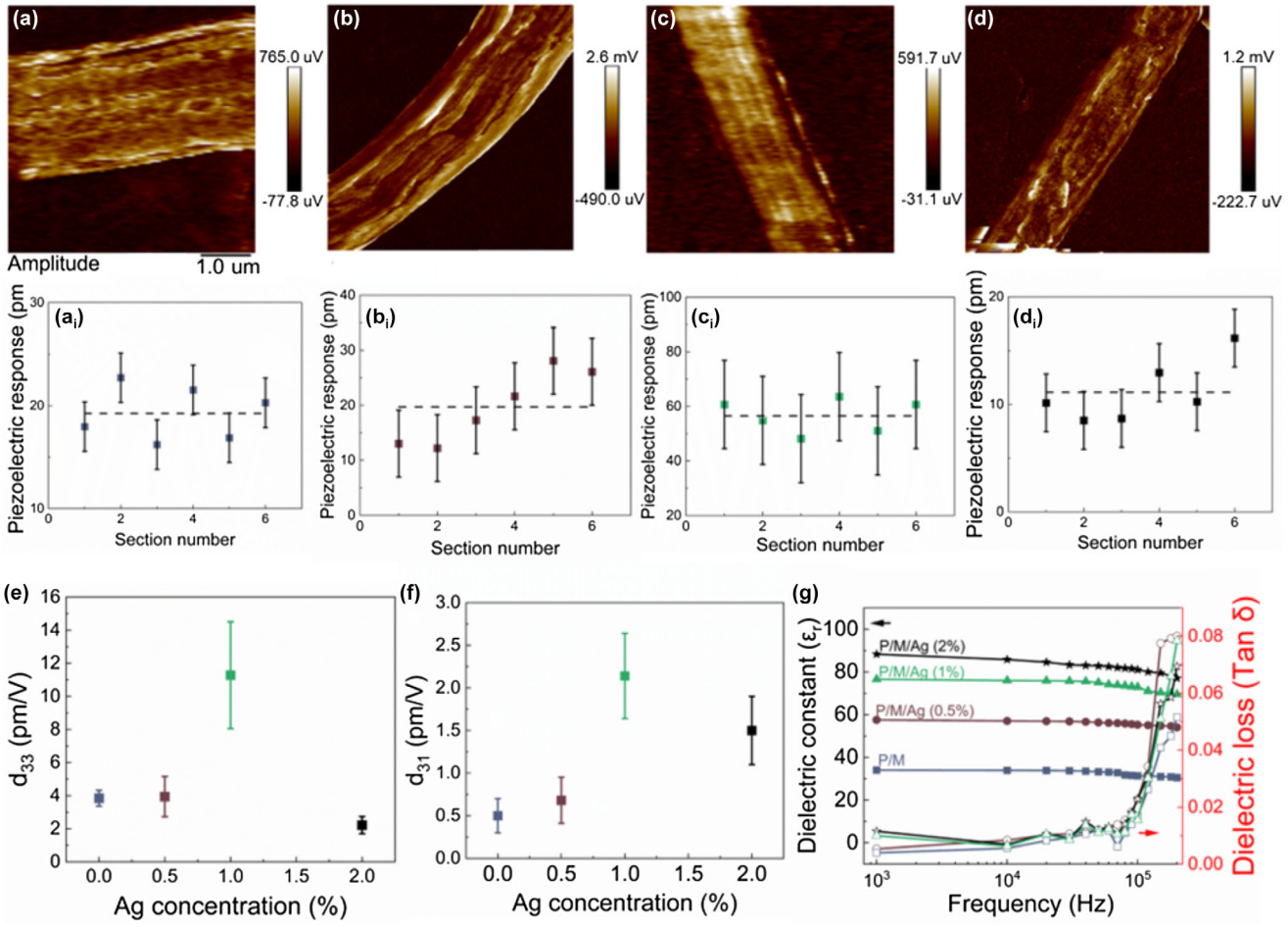

Figure 3. Piezoresponse force microscopy (PFM) images and averaged piezoelectric response value of poly(vinylidene fluoride-co-trifluoroethylene) (P(VDF-TrFE))/MXene containing various silver nanoparticles (AgNPs) concentrations: a) 0, b) 0.5, c) 1, d) 2 wt%, nanofibers deposited on an Au/Cr coated Si/SiO_2 wafer; calculated e) d_{33}, f) d_{31} value at different AgNPs contents, and g) dielectric constant and dielectric loss as a function of frequency for electrospun PVDF-TrFE/MXene mat with different AgNPs loadings.

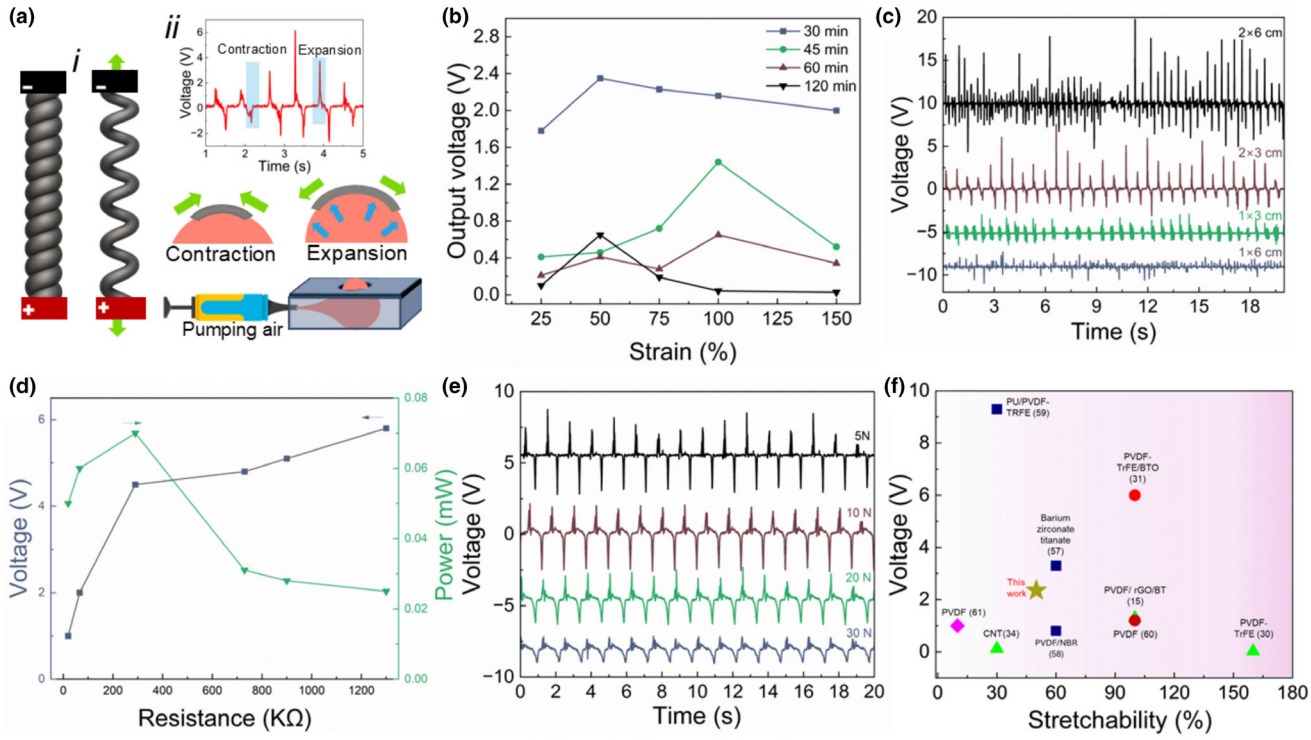

Figure 4. Schematic illustration of stimulating piezoelectric sensor: a_i) stretching coil structure in longitudinal direction with copper foil on both sides as electrodes, a_{ii}) simulation of heartbeat system using pressure of air balloon and the resultant strain waveform of the balloon surface for electrospun mat sensor, b) output voltage for various strains applied on 2 cm coils obtained from different electrospinning times, c) output voltage from sensors of different sizes under filled balloon pressure, d) the output voltage and power over load resistance of the sensor with a size of 2 × 3 cm under filled air balloon pressure, e) output voltage of sensor under different cyclic pressures in compression mode, and f) Comparison of the voltage and stretchability of piezoelectric generator in different structural designs of coil (▲), 3D printed (■), knitted (◆), and kirigami (●).[15,29,30,34,53–57]

applications such as pressure sensors, force sensors, and actuators where axial stress is dominant.[47,48] In contrast, a lower d_{31} (Figure 3f) coefficient reflects reduced transverse piezoelectric response, which can limit the material effectiveness in vibration sensing or energy harvesting applications that rely on lateral deformation.[49]

Figure 3g displays the frequency dependence of the dielectric constant (ε) and the tan δ of the nanocomposite electrospun mats. Across a frequency range of between 1 and 100 kHz, the trend of ε_r variation remains mostly consistent for all mats. The incorporation of AgNPs enhances interfacial polarization and facilitates the formation of a microcapacitor structure,[50] resulting in an increase in the ε value from 34 to 88. This is further supported by the decreased interlayer spacing between MXene flakes within the fiber structure as AgNP content increases, which promotes closer packing and more effective microcapacitor networks.[51] By increasing frequency, dielectric loss increases as a result of leakage current (conduction loss) in higher conductivity nanocomposite mats. There is a variation in tan δ values across different filler contents; however, the mat containing 1 wt% AgNP demonstrates optimal piezoelectric performance, exhibiting a high dielectric constant alongside a reduced dielectric loss.

2.3. Electromechanical Performance of Electrospun Mats and Coil Structures

Since stretchability is a critical property for wearable electronics, a dual strategy that combined innovative material selection with structural design was employed. For potential application in delivering charge to implanted pacemakers, two stimulation methods were investigated. The first involved mechanically stretching a coiled structure in the longitudinal direction under different strains (**Figure 4**a(i),b). The second involved sandwiching an electrospun mat between two layers of a conductive silver-coated nylon fabric, with the entire sensor encapsulated in PDMS. In this configuration, mechanical force was applied to the sensors by inflating an air-filled balloon, which was fixed at both ends within a sealed box. As the balloon expanded, a portion of it protruded through a circular hollow frame at the center of the box lid, exerting pressure on the sensor. This setup served to simulate periodic mechanical motion, mimicking the rhythmic behavior of a heartbeat at low strain in a radial direction[52] (Figure 4a(ii)).

As shown in Figure 4b, the coil structure fabricated from a 30 min electrospun mat produced an output voltage of 2.35 V under 50% strain (Figure S2, Supporting Information). As the strain increased to 150%, the output voltage decreased across all coil structures. The coil fabricated after 30 min of electrospinning generated approximately four times more voltage than the one produced after 120 min at the same 50% strain level. The power output of the coils was calculated using Equation (1):

$$P = \frac{1}{T}\int \frac{U^2(t)}{R}\,dt \qquad (1)$$

here, U(t) represents the real-time voltage, the frequency of the applied force is *T*, and the external load resistance is defined by *R*

(300 kΩ). At a frequency of 1 Hz and 50% strain, the 20 mm long P(VDF-TrFE)/MXene/AgNPs nanocomposite coil achieved a maximum power output of 18.4 μW and a power density of 6.6 mW cm^{-3}, approximately twice that reported in recent studies on piezoelectric nanogenerators.[58] The power output regarding the mass of the coil is 3.68 W kg^{-1}, which is 2.6 times higher than carbon nanotube coil.[34] The energy conversion efficiency from mechanical to electrical energy was 16.5%, calculated using Equation (2):

$$\eta = \frac{E_e}{E_m} \times 100 \quad (2)$$

here, E_e represents the total electrical output energy as defined in Equation (1), while E_m corresponds to the mechanical strain energy input during the coil axial stretching, determined by the force applied to the coil cross-sectional area at a specific strain level. The nanocomposite coil demonstrates an energy conversion efficiency nearly twice that of the latest reported values for electrical energy harvesting from polyurethane microfiber coils.[59]

Figure 4c illustrates the piezoelectric performance of the various rectangular sizes of the electrospun mat sensor under the stimulation conditions described in Figure 4a(ii). While the 2 × 6 cm sensor, which contains a greater quantity of active material, generates a higher output voltage, the 2 × 3 cm sensor demonstrates more consistent and reliable performance with an output power of 70 μW (Figure 4d). The dimensions of the piezoelectric sensor play a critical role in determining its output voltage. Larger sensors generate higher voltages under the same pressure due to their increased surface area and volume, which facilitates greater charge separation.[60] However, as the sensor length increases, mechanical deformation becomes more complex, often resulting in less consistent output voltage. For implantable devices, such as cardiac pacemakers designed to harvest energy from heartbeats, a sensor length of 3 cm is recommended to balance electrical performance, mechanical stability, and physiological compatibility.[34] Sensor performance was evaluated under different pressure levels, achieving a maximum voltage of 3 V at 1 Hz and a pressure of 7 kPa (Figure 4e). The fabricated piezoelectric generator, in both coil and film configurations, was able to generate sufficient voltage under induced strains in both the longitudinal and radial directions, confirming its potential for harvesting energy from cardiac muscle movements for charging implantable devices.

3. Conclusion

A bioinspired coil structure has been presented here as a framework to develop stretchable and flexible piezoelectric nanofibers based on $Ti_3C_2T_x$ MXene and AgNPs. These nanofibers were fabricated by electrospinning and exhibited excellent mechanical robustness to undergo twist insertion and form coils enduring an axial extension up to 200% strain. The addition of AgNPs into the P(VDF-TrFE)/$Ti_3C_2T_x$ MXene nanofibers was investigated for its effect on enhancing the piezoelectric coefficients in both longitudinal and transverse modes, resulting in an increase from 4 to 11.3 pC/N in the d_{33} coefficient with the addition of 1 wt% AgNPs. The coil structures exhibited a high power density of 6.6 mW cm^{-3} under periodic 50% strain. Among stretchable designs and compared to prior coil-structured materials, this design achieved superior output voltage generation (Figure 4f, Table S1, Supporting Information).

Our approach effectively balances flexibility, ease of fabrication, compactness, and high output voltage performance at low strain levels and low frequency. Our vision was to demonstrate the performance of piezoelectric structures in two different designs for energy harvesting: one operating under heart muscle contraction and relaxation (coil structure) and the other detecting heartbeats (nanofiber mat sensor), with the goal of overcoming the battery replacement challenge in implantable devices. The demonstrated material and coiled configuration offers a promising pathway for the miniaturization of energy harvesting devices for portable, self-powered biomedical implants such as cardiac pacemakers and wearable technologies.

4. Experimental Section

Materials: P(VDF-TrFE) powder (Piezotech FC25, France) was sourced from the Arkema Group, and silver nanoparticles (AgNPs) were provided by Inframat Advanced Materials Co., Ltd., USA. The Ti_3AlC_2 MAX phase was obtained from Carbon-Ukraine Ltd. Lithium fluoride (LiF, 99%), hydrochloric acid (HCl, 12 M), acetone, and N,N-dimethylformamide (DMF, ≥99%) were purchased from Sigma-Aldrich Pty Ltd. All chemicals were used as received without further purification. $Ti_3C_2T_x$ MXene was synthesized from the MAX phase precursor using the minimally intensive layer delamination (MILD) etching method (Figures S3 and S4, Supporting Information), yielding single-layer flakes, in accordance with our previously reported procedure.[14]

Electrospinning and coil fabrication: Electrospinning was carried out at an applied voltage of 18 kV with a feed rate of 0.8 mL h^{-1} onto aluminum foil. The needle-to-collector distance was maintained at 15 cm, and the fibers were collected on a grounded rotating drum operating at 100 rpm. To fabricate coils, electrospun mats obtained at different spinning durations (30, 40, 60, and 120 min) were cut into strips and twisted using a stepper motor. A small weight was attached to one end of each strip to ensure uniform coil formation. During the twisting process, the coil began to form from one end of the ribbon and gradually extended to the opposite end, ultimately resulting in a fully packed coil. While both ends of the coils were clamped to prevent loss of twist, the samples were annealed at 90 °C in an isothermal oven to permanently fix the coiled structure. After 60 min of heating, the coils were removed and allowed to relax for 2 h at room temperature, with clamps still in place to maintain their shape.

Characterization: Fourier-transform infrared (FTIR) spectroscopy was conducted using an Agilent Cary 630 FTIR spectrometer. Differential scanning calorimetry (DSC) analysis was performed with a Netzsch DSC 214 Polyma instrument. Approximately 5 mg of fiber material was accurately weighed and sealed in an aluminum crucible. The sample was then placed in the instrument furnace, which was purged with nitrogen at a flow rate of 40 mL min^{-1}. Heating was performed at a rate of 5 °C min^{-1} up to at least 250 °C. Peak temperatures and enthalpies were analyzed using the Proteus software (Netzsch, Germany). Mechanical testing was carried out using an Instron 5943 universal testing machine equipped with pneumatic clamp with a 100 N load cell at a constant tensile strain rate of 5 mm min^{-1}. All samples were sputter-coated with gold (Balzers, Switzerland) for 45 s at 20 mA, degassed in a vacuum chamber, and then examined for surface morphology using a FEI XL30 FEG SEM (Philips, the Netherlands) operated at an accelerating voltage of 10 kV and a working distance of approximately 10 mm. Fiber diameters were measured from SEM images using ImageJ software. Phase structure was analyzed using X-ray diffraction (XRD) with the Bruker D2 Phaser goniometer equipped with a Cu-tube for diffraction measurements with an acceleration voltage of 30 kV and a current of 10 mA. The dielectric constant (ε_r) and loss tangent (tanδ) were measured over a frequency range of 1–100 kHz using a Rohde & Schwarz HAMEG LCR precision impedance analyzer (Germany).

Piezoelectric force microscopy measurement: Piezoresponse force microscopy (PFM) measurements were performed by using a MultiMode 8 (Bruker, USA) equipped with a PFM module. In order to minimize the electrostatic contribution to the piezoresponse (PR) signal, the relatively stiff conductive platinum silicide probes PtSi-FM from "Nanosensors" (force constant ~4 N m^{-1}) were used. With the further aim of reducing the influence of the parasitic AC electrostatic field, quantitative measurements were carried out with an applied DC voltage of

−0.1 to −0.3 V. This voltage was adjusted to correspond to the minimum value of the contact resonance response of the probe. To induce PR, an AC voltage was applied at a frequency of 8.9 kHz between the probe and the conductive substrate with the deposited nanofibers. PR signal was detected by Lock-in. The AC voltage dependencies of PR were measured and, as expected, a linear response was observed without irreversibility up to an AC voltage amplitude of 10 V (Figure S1, Supporting Information). It should be noted that the use of a relatively low frequency for PR measurements and the mentioned procedure for adjusting the DC-bias made it possible to significantly reduce the influence of parasitic electrostatic effects, which was expressed in the passage of the PR dependence lines practically through the origin of coordinates. The presented measurement results were obtained at an AC voltage of 5 V. The calibration of the PFM response was carried out using a periodically poled single-crystal sample of "Bruker SMPL $LiNbO_3$" (Bruker, USA).

Acknowledgements

F.M. acknowledges financial support received from the European Commission through Marie Skłodowska-Curie Actions (MSCA) fellowship (2024). The authors acknowledge the KU Leuven Electron Microscopy facility. . Open access publishing facilitated by RMIT University, as part of the Wiley - RMIT University agreement via the Council of Australasian University Librarians

Conflict of Interest

The authors declare no conflict of interest.

Supporting Information

Supporting Information is available from the Wiley Online Library or from the author.

Keywords

coil structure, MXene, nanogenerator, piezoelectric nanofibers, sustainable energy

Received: November 20, 2025
Revised: January 27, 2026
Published online: February 13, 2026

[1] W. Tang, Q. Sun, Z. L. Wang, *Chem. Rev.* **2023**, *123*, 12105.
[2] F. Mokhtari, A. Samadi, A. O. Rashed, X. Li, J. M. Razal, L. Kong, R. J. Varley, S. Zhao, *Prog. Mater. Sci.* **2025**, *148*, 101376.
[3] F. Mokhtari, H. Y. Nam, A. Ruhparwar, R. Raad, J. M. Razal, R. J. Varley, C. H. Wang, J. Foroughi, *J. Mater. Chem. B* **2024**, *12*, 9727.
[4] M. Khazaee, M. Hasani, A. A. Enkeshafi, S. Riahi, K. Pedersen, A. Rezania, *Smart Mater. Struct.* **2025**, *34*, 055016.
[5] J. F. Hou, M. O. G. Nayeem, K. A. Caplan, E. A. Ruesch, A. Caban-Murillo, E. Criado-Hidalgo, S. B. Ornellas, B. Williams, A. A. Pearce, H. E. Dagdeviren, M. Surets, J. A. White, M. G. Shapiro, F. Wang, S. Ramirez, C. Dagdeviren, *Nat. Commun.* **2024**, *15*, 4601.
[6] F. Mokhtari, S. Danti, B. Azimi, F. Hellies, E. Zanoletti, G. Albertin, L. Astolfi, R. J. Varley, J. M. Razal, *Energy Environ. Mater.* **2025**, *8*, e12807.
[7] A. Yuvarajan, G. Vishnu, N. Saranraj, *Biomed. Mater. Devices* **2025**, *1*, 312.
[8] N. Almarri, J. Chang, W. Song, D. Jiang, A. Demosthenous, *Nano Energy* **2024**, *131*, 110196.
[9] F. Mokhtari, P. Heidarian, R. J. Varley, J. M. Razal, in *Energy Harvesting Properties of Electrospun Nanofibers*, 2nd ed. (Eds: T. Lin, J. Fang), IOP Publishing, Bristol, UK **2025**, pp. 5-1–5-22.
[10] K. O. Iwuozor, T. A. Jimoh, H. T. Ojo, E. C. Emenike, J. Emeghai, A. G. Adeniyi, *Surf. Interfaces* **2025**, *70*, 106855.
[11] F. Mokhtari, M. Shamshirsaz, M. Latifi, S. Asadi, *J. Tex. Institute* **2017**, *108*, 906.
[12] C. Shee, S. Banerjee, S. Bairagi, A. Baburaj, K. S. K. Naveen, A. K. Aliyana, D. M. Mulvihill, R. Alagirusamy, S. W. Ali, *J. Phys. Energy* **2024**, *6*, 032001.
[13] Z. Li, X. Wang, Y. Lu, Y. Liu, *Mater. Res. Bull.* **2025**, *185*, 113276.
[14] F. Mokhtari, K. A. S. Usman, J. Zhang, R. Komljenovic, Ž. Simon, B. Dharmasiri, A. Rezk, P. C. Sherrell, L. C. Henderson, R. J. Varley, J. M. Razal, *ACS Appl. Mater. Interfaces* **2025**, *17*, 3214.
[15] F. Mokhtari, G. M. Spinks, S. Sayyar, Z. Cheng, A. Ruhparwar, J. Foroughi, *Adv. Mater. Technol.* **2021**, *6*, 2000841.
[16] H. Khatun, C. Sharma, U. Sarma, *Sens. Actuators A Phys.* **2025**, *392*, 116723.
[17] A. Aishwarya, S. Mondal, N. Bhattacharjee, T. Dasgupta, A. R. Bhattacharyya, *Polym. Compos.* **2025**, *46*, 8533.
[18] A. Ali, S. Iqbal, X. Chen, *Energ. Strat. Rev.* **2024**, *53*, 101422.
[19] F. Mokhtari, T. Groetsch, P. Heidarian, M. Maghe, R. J. Varley, *Macromol. Rapid Commun.* **2025**, *46*, e00429.
[20] R. Qin, J. Nong, K. Wang, Y. Liu, S. Zhou, M. Hu, H. Zhao, G. Shan, *Adv. Mater.* **2024**, *36*, 2312761.
[21] B. S. Athira, K. P. Surendran, A. Chandran, *Chem. Eng. J.* **2025**, *506*, 160056.
[22] Y. Ao, L. Jin, S. Wang, B. Lan, G. Tian, T. Xu, L. Huang, Z. Wang, Y. Sun, T. Yang, W. Deng, F. Yang, W. Yang, *Nano Micro Lett.* **2025**, *17*, 320.
[23] C.-T. Pan, K. Dutt, A. Kumar, R. Kumar, C.-H. Chuang, Y.-T. Lo, Z.-H. Wen, C.-S. Wang, S.-W. Kuo, *Int. J. Bioprint.* **2022**, *9*, 647.
[24] L. Kang, S. Huang, X. Qin, X. Gao, Y. Li, X. Zhang, *ACS Appl. Nano Mater.* **2024**, *7*, 9252.
[25] W. Fan, R. Lei, H. Dou, Z. Wu, L. Lu, S. Wang, X. Liu, W. Chen, M. Rezakazemi, T. M. Aminabhavi, Y. Li, S. Ge, *Nat. Commun.* **2024**, *15*, 3509.
[26] W. Qian, K. Zhao, D. Zhang, C. R. Bowen, Y. Wang, Y. Yang, *ACS Appl. Mater. Interfaces* **2019**, *11*, 27862.
[27] B. Wu, L. Wang, H. Xu, D. Zhang, J. Kang, Y. Yang, K. Yin, M. Nie, L. Sun, *Chem. Eng. J.* **2025**, *510*, 161325.
[28] D. Zhang, H. Sun, M. Huang, M. Su, Y. Ma, M. Shi, L. Mi, C. Liu, H. Liu, *Chem. Eng. J.* **2024**, *496*, 153752.
[29] L. Zhao, S. Yu, J. Li, Z. Song, M. Wu, X. Wang, X. Wang, *J. Mater. Chem. C* **2021**, *9*, 13886.
[30] M. Baniasadi, J. Huang, Z. Xu, S. Moreno, X. Yang, J. Chang, M. A. Quevedo-Lopez, M. Naraghi, M. Minary-Jolandan, *ACS Appl. Mater. Interfaces* **2015**, *7*, 5358.
[31] X. Zhou, K. Parida, O. Halevi, Y. Liu, J. Xiong, S. Magdassi, P. S. Lee, *Nano Energy* **2020**, *72*, 104676.
[32] F. Xu, J. Yang, R. Dong, H. Jiang, C. Wang, W. Liu, Z. Jiang, X. Zhang, G. Zhu, *Adv. Fiber Mater.* **2021**, *3*, 368.
[33] M. Cheng, K. Tian, T. Qin, Q. Li, H. Deng, Q. Fu, *SusMat* **2024**, *4*, e204.
[34] A. Ruhparwar, A. Osswald, H. Kim, R. Wakili, J. Müller, N. Pizanis, F. Al-Rashid, U. Hendgen-Cotta, T. Rassaf, S. J. Kim, *Adv. Mater.* **2024**, *36*, 2313688.
[35] J. Li, S. Wang, H. Lu, Y. Tu, X. Wan, X. Li, Y. Tu, C. Y. Li, *ACS Macro Lett.* **2023**, *12*, 369.
[36] J. Li, C. Xie, W. Liu, L. Sun, Y. Gao, Z. Lu, F. Xu, W. Liu, *J. Appl. Polym. Sci.* **2025**, *142*, e57586.
[37] F. Mokhtari, R. W. Symes, Ž. Simon, B. Dharmasiri, L. C. Henderson, M. W. Joosten, R. J. Varley, *J. Mater. Chem. A* **2025**, *13*, 6482.
[38] T. Liu, F. Xie, L. Geng, R. He, M. Sun, T. Ni, P. Xu, C. Xing, Y. Peng, K. Chen, Y. Fang, *Int. J. Nanomedicine* **2025**, *20*, 771.

[39] Y. Shi, H. Chen, X. Guan, *Polym. Test.* **2021**, *101*, 107277.
[40] S. Suresh, B. S. Athira, N. S. Akhila, L. Vijaya, A. Chandran, E. B. Gowd, *ACS Appl. Mater. Interfaces* **2025**, *17*, 9818.
[41] M. Krutko, H. M. Poling, M. Sheth, S. Kongsomros, A. E. Bryan, M. Sharma, A. Singh, H. A. Reza, K. A. Wikenheiser-Brokamp, T. Takebe, M. A. Helmrath, G. M. Harris, L. Esfandiari, *Adv. Mater. Technol.* **2025**, *10*, e01513.
[42] A. Mankuni, S. Varghese, *ACS Appl. Electron. Mater.* **2024**, *6*, 4194.
[43] N. Alnairat, M. Abu Dalo, R. Abu-Zurayk, S. Abu Mallouh, F. Odeh, A. Al Bawab, *Polymers* **2021**, *13*, 3683.
[44] X. Liu, J. Tong, J. Wang, S. Lu, D. Yang, H. Li, C. Liu, Y. Song, *J. Mater. Chem. C* **2023**, *11*, 4614.
[45] Y. Zeng, L. Tang, *Polym. Compos.* **2025**, *46*, 10636.
[46] Y. Huang, J. Zhang, L. An, Y. Yang, Y. Wu, R. Liu, Y. Jin, Q. Liu, Q. Shi, Y. Liang, *Polymer* **2023**, *286*, 126399.
[47] G. M. Spinks, B. B. A. Abbasi, A. Gautam, F. Mokhtari, Z. Jiang, *Adv. Mater. Technol.* **2023**, *8*, 2202101.
[48] C. D. Fay, N. Mannering, A. Jeiranikhameneh, F. Mokhtari, J. Foroughi, R. H. Baughman, P. F. M. Choong, G. G. Wallace, *Adv. Sensor Res.* **2023**, *2*, 2200021.
[49] S. B. Kim, H. Park, S. H. Kim, H. C. Wikle, J. H. Park, D. J. Kim, *J. Microelectromech. Syst.* **2013**, *22*, 26.
[50] T. Sun, C. Cai, J. Guo, B. Zhu, X. Chen, Y. He, W. Zhong, R. He, L. Ye, J. Zhang, S. Ma, *Polym. Compos.* **2026**, *47*, 470.
[51] W. Ma, K. Yang, H. Wang, H. Li, *ACS Appl. Nano Mater.* **2020**, *3*, 7992.
[52] X. Papademetris, J. Duncan, in *Handbook of Medical Imaging*, Vol. 2 (Eds: M. Sonka, J. M. Fitzpatrick), SPIE PRESS, Bellingham, Washington, USA **2000**.
[53] Q. Xu, Y. Tao, Z. Wang, H. Zeng, J. Yang, Y. Li, S. Zhao, P. Tang, J. Zhang, M. Yan, Q. Wang, K. Zhou, D. Zhang, H. Xie, Y. Zhang, C. Bowen, *Adv. Mater.* **2024**, *36*, 2311624.
[54] R. Tu, H. A. Sodano, *ACS Appl. Mater. Interfaces* **2023**, *15*, 22320.
[55] S. Siddiqui, H. B. Lee, D.-I. Kim, L. T. Duy, A. Hanif, N.-E. Lee, *Adv. Energy Mater.* **2018**, *8*, 1701520.
[56] Y. G. Kim, S. Hong, B. Hwang, S. H. Ahn, J. H. Song, *Sci. Rep.* **2022**, *12*, 19149.
[57] F. Mokhtari, G. M. Spinks, C. Fay, Z. Cheng, R. Raad, J. Xi, J. Foroughi, *Adv. Mater. Technol.* **2020**, *5*, 1900900.
[58] S. An, X. Gao, M. Zheng, M. Zhang, P. Liu, M. Zhu, Y. Hou, *Nano Energy* **2024**, *123*, 109420.
[59] S. H. Kim, H. J. Sim, J. S. Hyeon, D. Suh, G. M. Spinks, R. H. Baughman, S. J. Kim, *Sci. Rep.* **2018**, *8*, 8712.
[60] S. Wang, C. Wang, H. Yuan, X. Ji, G. Yu, X. Jia, *Appl. Energy* **2023**, *330*, 120379.